INSTITUTE OF PHYSICS PUBLISHING JOURNAL OF MICROMECHANICS AND MICROENGINEERING

J. Micromech. Microeng. **16** (2006) 303–313 doi:10.1088/0960-1317/16/2/015

Simple models for piston-type micromirror behavior

M H Miller[1], J A Perrault[2], G G Parker[1], B P Bettig[1] and T G Bifano[2]

[1] Michigan Technological University, 1400 Townsend Drive, Houghton, MI 49931, USA

[2] Boston University, 15 St Mary's Street, Brookline, MA 02446, USA

E-mail: mhmiller@mtu.edu

Received 7 September 2005, in final form 9 December 2005
Published 9 January 2006
Online at stacks.iop.org/JMM/16/303

Abstract

Parallel-plate electrostatic actuators are a simple way to achieve piston motion for large numbers of mirrors in spatial light modulators. However, selection of design parameters is made difficult by their nonlinear behavior. This paper presents simple models for predicting static and dynamic behaviors of fixed–fixed parallel-plate electrostatic actuators. Static deflection equations are derived based on minimization of the total potential energy of the beam. Beam bending, residual stress, beam stretch and applied electrostatic force are included in the potential energy formulation. Computation time is reduced by working with assumed mode shapes. The problem of predicting midpoint beam deflection has been reduced to finding the roots of a third-order equation. Model results are compared to finite-element analysis results. In the dynamic analysis, Lagrange's method is used to derive the nonlinear equation of motion. An equation for predicting natural frequency, assuming small midpoint deflections about a dc setpoint, is presented. In addition, the effect of gas pressure on the damped natural frequency of a rigid actuator is analyzed. Experimental measurements of static deflection and frequency response are compared to model predictions. The actual micromirrors exhibit less strain stiffening than the model predicts.

(Some figures in this article are in colour only in the electronic version)

1. Introduction

Large arrays of micromachined piston-motion mirrors are required for laser communication and optical correlation applications. Such devices can be used to rapidly modify the spatial phase of a coherent wavefront. Spatial phase modulation has been possible for some years, primarily through the use of liquid crystal phase devices. MEMS-based spatial light modulators (μSLM) promise orders of magnitude higher speed, enabling the use of SLMs in applications such as pattern recognition and laser communication, which typically require faster response than is achievable using liquid crystal devices. In the design of these devices mirror flatness, maximum static deflection and response time are specified. For our specific application, maximum deflection was specified as 750 nm and step response time as 10 μs.

An efficient way to accomplish the piston motion of the SLM pixels is via parallel-plate electrostatic actuators. This design is easy to fabricate and permits a high fill factor mirror surface. While the basic operation of a parallel-plate electrostatic actuator is simple, its static and dynamic behaviors are complex to model.

A wide spectrum of analytical and numerical models has been developed for describing the motion of parallel-plate electrostatic actuators. Beam bending models have been modified to include the nonlinear electrostatic force, stiffening due to beam stretch and residual stress from the fabrication process. The models are commonly used to predict static deflection, pull-in voltage and resonant frequency. Tilmans and Legtenberg [1] use the Rayleigh–Ritz energy minimization with versine and dynamic mode shapes to predict pull-in voltage and resonant frequency of electrostatically driven

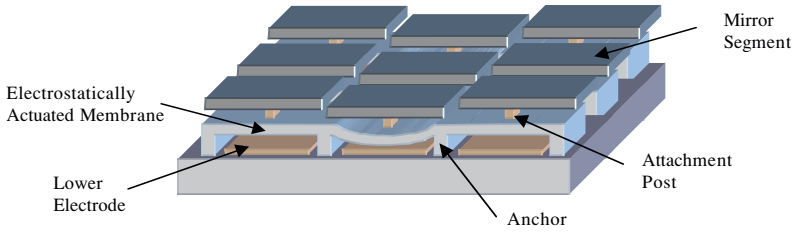

Figure 1. Schematic of nine elements in a micromachined spatial light modulator (μSLM).

resonators. They describe the effect of dc bias voltage on resonant frequency. Their model does not include beam stretch. Choi and Lovell [2] use a shooting method to solve the nonlinear force equilibrium equation. They noted the significant effects of beam stretch and residual stress on static displacement. Najar *et al* [3] use the differential quadrature method to discretize the beam equation of motion. Abdel-Rahman *et al* [4] present a detailed parametric analysis of the beam stretch effect.

Several strategies have been adopted to reduce computation time. Choi and Lovell [2] derived a closed form solution for the actuator displacement based on one- and two-term linear approximations of the electrostatic force. Chowdhury *et al* [5] describe a semi-empirical closed form model for the pull-in voltage. Ananthasuresh *et al* [6] investigated the relationship between number of mode shapes and accuracy of reduced-order macromodels. Mehner *et al* [7] describe a process for generating macromodels based on modal methods and polynomial fits of finite-element results. Younis *et al* [8] generated a reduced-order model by using up to five linear undamped dynamic mode shapes to represent the beam.

Ambient pressure of the operating environment has a significant effect on dynamic behavior. A number of researchers have experimentally observed the effect of gas pressure on resonant frequency for MEMS devices, including Seidel *et al* [9], Andrews *et al* [10] and Veijola *et al* [11]. Squeeze film dynamics models adequately characterize the observed behaviors. Yang *et al* [12] present a model of squeeze film damping for flexible beams. Hung *et al* [13] describe a method for generating orthogonal basis functions for actuator shape and air pressure from results of a small number of high-order dynamical simulations. Darling *et al* [14] developed computationally efficient equations for rigid plates with arbitrary venting conditions. By using perturbation methods to derive analytical expressions for the gas pressure distribution, Nayfeh and Younis [15] improve the accuracy of models that apply to flexible beams.

Our goal is to develop simple equations that permit accurate quick predictions of micromirror deflection and bandwidth. The models must accurately account for the effects of dc bias voltage and ambient pressure. While adopting oft-used approaches, such as energy minimization, assumed modes and the Lagrangian method, we consider a unique set of assumed modes and account for the extra mass of the mirror layer. We carry out finite-element simulations and measure performance of micromirror devices for comparison.

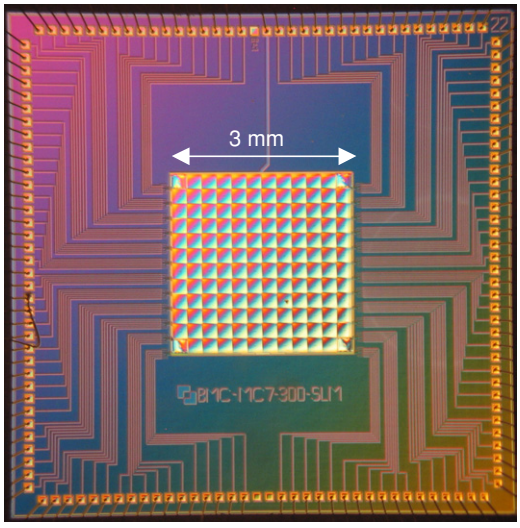

Figure 2. Nomarski micrograph of 140 pixel μSLM.

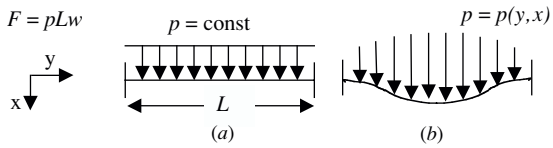

Figure 3. Fixed–fixed beam bending under (*a*) uniform distributed load and (*b*) non-uniform distributed load.

2. Static analysis

Nine pixels of a μSLM device are shown schematically in figure 1. The complete device may have hundreds or thousands of such pixels. A device similar to that shown in figure 2 was used for the experimental testing described in sections 3, 5 and 6. A pixel is actuated by applying a voltage difference between its membrane and the lower electrode.

The electrostatic force can be described by

$$F_{\text{electrost}} = \frac{\varepsilon_o A V^2}{2(g_o - x)^2}, \tag{1}$$

where ε_o is the permittivity of free space, A is the electrode area, V is the voltage difference, g_o is the original gap and x is the actuator displacement.

The membrane layer may be modeled as a fixed–fixed beam with distributed load. Figure 3(*a*) shows a uniform distributed load for which the stiffness can be modeled as

$$k = 384\frac{EI}{L^3}. \tag{2}$$

Table 1. Beam mode shapes used in static deflection analysis.

$\phi(y) = y^4 - 2Ly^3 + L^2y^2$	Uniform load
$\phi(y) = -\frac{1}{360}y^6 + \frac{1}{120}Ly^5 - \frac{5}{360}L^3y^3 + \frac{1}{120}L^4y^2$	Parabolic load
$\phi(y) = \left(\cosh\frac{\lambda y}{L} - \cos\frac{\lambda y}{L}\right) - \frac{\cos\lambda - \cosh\lambda}{\sin\lambda - \sinh\lambda}\left(\sinh\frac{\lambda y}{L} - \sin\frac{\lambda y}{L}\right)$	Dynamic ($\lambda = 4.73$)
$\phi(y) = 1 - \cos\frac{2\pi y}{L}$	Versine

Figure 3(*b*) shows the more realistic non-uniform load that results from the deflection x dependence in the electrostatic force.

The static deflection of the beam can be found by minimizing the total potential energy of the beam, π:

$$\pi = \underbrace{\frac{EI}{2}\int_0^L (x'')^2\,\mathrm{d}y}_{\text{bending}} + \underbrace{\frac{EA}{8}\int_0^L (x')^4\,\mathrm{d}y}_{\text{beam stretch}} - \underbrace{\frac{F_a}{2}\int_0^L (x')^2\,\mathrm{d}y}_{\text{residual axial stress}} - \underbrace{\frac{\varepsilon_o w V^2}{2}\int_0^L \frac{1}{g_o - x}\,\mathrm{d}y}_{\text{electrostatic force}}, \tag{3}$$

where EI is the beam's flexural rigidity, $x(y)$ its deflection, F_a is the applied axial compressive force, ε_o is the permittivity of free space (8.854×10^{-12} C^2 N^{-1} m^{-2}), L is the length of the beam, w is the width of the beam and g_o is the nominal gap between the bottom of the beam and the stationary plate below.

2.1. Assumed modes

The shape of the actuator membrane during deflection can be accurately described with finite-element methods. To reduce computation time, we solved equation (3) by assuming mode shapes with the following form:

$$x(y) = \sum_i a_i \phi_i(y). \tag{4}$$

To find the beam deflection given the mode shapes ϕ_i and input voltage V, it would then be necessary to find the constants a_i that minimize π in equation (3). Table 1 describes four types of mode shapes that were considered both individually and in combination. The uniform and parabolic load modes are the shapes that result from solving the static beam deflection equation

$$EI\phi'''' = \int_0^L p(y)\,\mathrm{d}y \tag{5}$$

for a fixed–fixed cantilever beam with distributed pressure $p =$ constant and $p =$ parabola, respectively. The dynamic mode shape is the first dynamic mode for a fixed–fixed cantilever beam. The versine model shape has no physical significance other than that it satisfies the boundary conditions and has a reasonable shape. Figure 4 compares the four mode shapes. All are very similar, especially the first three.

The beam deflection can be estimated by finding a_is that minimize π in equation (3) or finding as that solve

$$\nabla\pi = 0. \tag{6}$$

As an example, consider a one-mode expansion of x:

$$x(y) = a\phi(y), \tag{7}$$

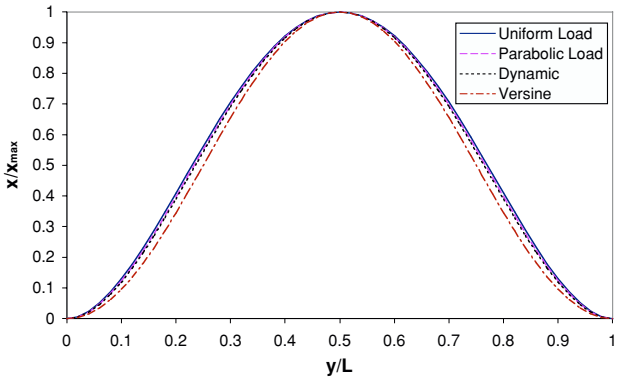

Figure 4. Comparison of analytical mode shapes.

where $\phi(y)$ is one of the mode shapes described above. Then equation (3) becomes

$$\pi = a^2\frac{EI}{2}\int_0^L (\phi'')^2\,\mathrm{d}y + a^4\frac{EA}{8}\int_0^L (\phi')^4\,\mathrm{d}y - a^2\frac{F_a}{2}\int_0^L (\phi')^2\,\mathrm{d}y - \frac{\varepsilon_o w V^2}{2}\int_0^L \frac{1}{g_o - a\phi}\,\mathrm{d}y. \tag{8}$$

Substituting equation (8) into equation (6) yields

$$\frac{\mathrm{d}\pi}{\mathrm{d}a} = 0 = aEI\int_0^L (\phi'')^2\,\mathrm{d}y + a^3\frac{EA}{2}\int_0^L (\phi')^4\,\mathrm{d}y - aF_a\int_0^L (\phi')^2\,\mathrm{d}y - \frac{\varepsilon_o w V^2}{2}\int_0^L \frac{\phi}{(g_o - a\phi)^2}\,\mathrm{d}y. \tag{9}$$

2.2. Numerical solution

The electrostatic (last) term in equation (9) prevents an analytical solution. Using a numerical minimization routine, a in equation (8) can be found and then substituted back into equation (7) to yield the beam deflection.

Deflections were found in this way for the four mode shapes using the conditions given in table 2. The actuator dimensions listed in table 2 coincide with the dimensions of the actual device used later for experimental validation. The beam was discretized into 400 elements when performing the numerical integrations. Figure 5 shows the midpoint deflections for the numerical integration results. The results for the four mode shape assumptions are nearly identical to each other up to about 175 V.

Two-term combinations of mode shapes were also tried, such as

$$x(y) = a_1\phi_{\text{uniform}} + a_2\phi_{\text{dynamic}}. \tag{10}$$

These results differed from those shown in figure 5 by a negligible amount.

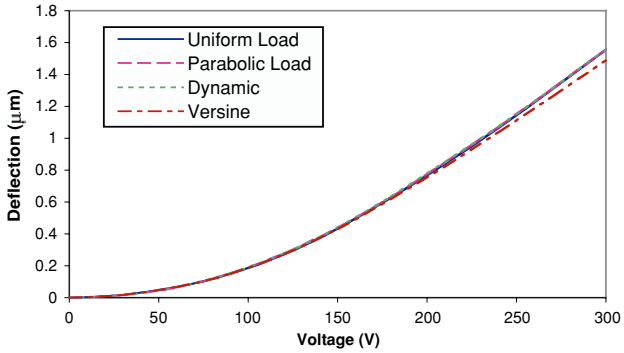

Figure 5. Comparison of midpoint deflections resulting from the numerical solution with different mode shape assumptions.

Table 2. Conditions for the case study.

Parameter	Value
Elastic modulus (E)	170 GPa
Density (ρ)	2330 kg m^{-3}
Length (L)	240 μm
Width (w)	240 μm
Thickness (t)	2 μm
Nominal gap (g_o)	5 μm
Axial pressure ($F_a/(wt)$)	10 MPa
Permittivity (ε_o)	8.854×10^{-12} C^2 N^{-1} m^{-2}

2.3. Approximate solution

A binomial series expansion of the electrostatic force term in equation (9) permits an analytical solution. We wanted to determine the number of terms that would give adequate deflection predictions. The integrand of the last term in equation (9) can be approximated as follows:

$$\frac{\phi}{(g_o - a\phi)^2} = \frac{\phi}{g_o^2\left(1 - \frac{a\phi}{g_o}\right)^2} = \frac{\phi}{g_o^2}\left[1 + 2\frac{a\phi}{g_o} + 3\left(\frac{a\phi}{g_o}\right)^2 + 4\left(\frac{a\phi}{g_o}\right)^3 + \cdots\right]. \tag{11}$$

Substituting equation (11) into equation (9) gives

$$0 = \underbrace{-\frac{\varepsilon_o w V^2}{2g_o^2}\int_0^L \phi \, dy}_{\text{zeroth-order term}} + \left[EI\int_0^L (\phi'')^2 \, dy - F_a\int_0^L (\phi')^2 \, dy - \underbrace{\frac{\varepsilon_o w V^2}{g_o^3}\int_0^L \phi^2 \, dy}_{\text{first-order term}}\right] a - \underbrace{\left[\frac{3\varepsilon_o w V^2}{2g_o^4}\int_0^L \phi^3 \, dy\right]}_{\text{second-order term}} a^2 + \left[\frac{EA}{2}\int_0^L (\phi')^4 \, dy - \underbrace{\frac{2\varepsilon_o w V^2}{g_o^5}\int_0^L \phi^4 \, dy}_{\text{third-order term}}\right] a^3 - \cdots - \underbrace{\left[\frac{n+1}{2g_o^{n+2}}\varepsilon_o w V^2 \int_0^L \phi^{n+1} \, dy\right]}_{n\text{th-order term}} a^n. \tag{12}$$

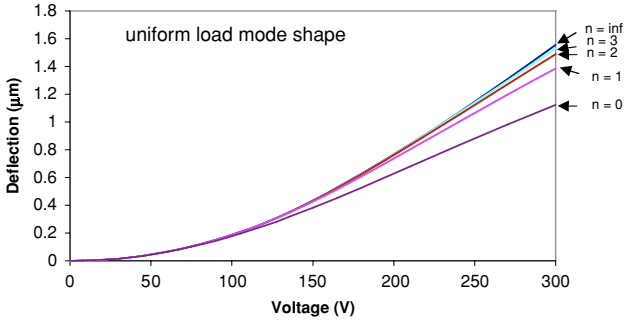

Figure 6. Midpoint deflection prediction using zeroth–third-order expansions of the electrostatic force term.

The coefficients of a in this equation can readily be calculated and the roots of a found. The midpoint deflection of the beam is

$$x(L/2) = a\phi(L/2). \tag{13}$$

For example, for the uniform load mode shape, equation (12) is

$$0 = \underbrace{-\frac{\varepsilon_o w V^2}{60g_o^2}}_{\text{zeroth-order term}} + \left(\frac{4EI}{5} - \frac{2F_a L^2}{105} - \underbrace{\frac{\varepsilon_o w V^2 L^4}{630 g_o^3}}_{\text{first-order term}}\right) a - \underbrace{\left(\frac{\varepsilon_o w V^2 L^8}{8008 g_o^4}\right) a^2}_{\text{second-order term}} + \left(\frac{4EAL^8}{15\,015} - \underbrace{\frac{\varepsilon_o w V^2 L^{12}}{109\,395 g_o^5}}_{\text{third-order term}}\right) a^3 \tag{14}$$

and the midpoint deflection is

$$x_{L/2} = \frac{L^4}{16} a. \tag{15}$$

Figure 6 shows the midpoint beam deflection assuming a uniform load mode shape for $n = 0$–3 as well as $n =$ infinity (equivalent to the numerical integration solution for uniform load mode shape shown in figure 5). Note that at 150 V the third-order expansion has 0.20% error while the first-order expansion has 1.6% error. At 300 V, the error with the third-order expansion is 1.6%. It is 11% for a first-order expansion and 28% for a zeroth-order expansion.

3. Static model validation

A finite-element model was created for comparison to the uniform load mode shape solution. It consisted of 96 × 96 linear quadrilateral plate elements for the actuator membrane. The two end supports were either assumed rigid or modeled with 8 × 96 × 2 linear solid hexahedron elements. Figure 7 compares the midpoint deflection results for the conditions described in table 2, assuming rigid supports. The results match very closely up to an input voltage of 180 V (0.6 μm deflection).

At higher deflections, the uniform mode shape assumption begins to break down. To explore this further, the shape along the centerline of the finite-element plate was recorded for several applied voltage/deflection conditions. Figure 8 compares the uniform load mode shape (that is independent

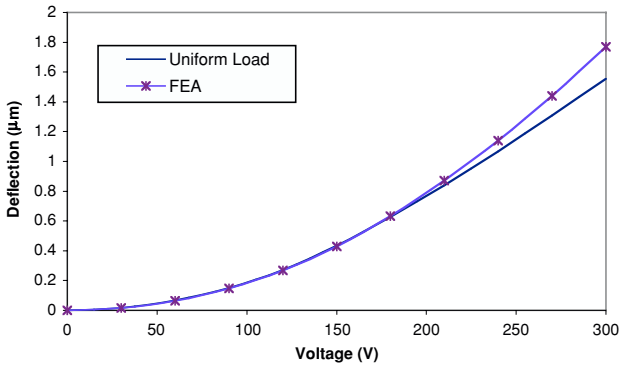

Figure 7. Comparison of midpoint deflection results for conditions outlined in table 2.

of voltage/deflection) with finite-element mode shapes for two voltage/deflection conditions. Note that both finite-element shapes are nearly identical to the uniform mode shape; however, the finite-element shape drifts away from the uniform load mode shape at higher deflections. Mehner *et al* [7] note that higher order mode shapes are necessary to adequately capture beam shape at higher deflections.

Static midpoint deflection of a 5 μm gap actuator with mirror (such as that depicted in figure 1) was measured using a white light interferometer. Table 3 lists the actuator design dimensions (similar to the case study described in table 2). Actual devices are subject to manufacturing variations that will affect device behavior. Thus, the table also cites the process standard deviation for two critical dimensions (actuator thickness and gap height). The mirror is connected to the actuator by an attachment post. The anchors on the two ends of the actuator are 240 μm long and 80 μm wide. They consist of captured PSG oxide (232 μm $\times$ 72 μm) surrounded by a 4 μm wide wall of polysilicon.

Predicting the deflection based on the above analysis method requires an assumption about the compressive residual stress. Figure 9 shows a comparison of measured static deflection data and predicted deflection assuming a residual compressive stress of 29 MPa. The solid 'modeled' curve is based on equation (14). Note that stiffening due to beam stretch tends to flatten the curve to an extent not seen in the experimental data. The FEA result with rigid supports is also shown. The FEA result does not agree with the modeled result as well as in figure 7 because the high residual stress (29 MPa) alters the FEA mode shape to an extent that it does not match the uniform load mode shape as closely. Similar to the 'modeled' curve, the 'FEA, rigid supports' curve is much flatter than the experimental one. Next, we modified the FEA result to allow the end support structures to deflect. As shown in figure 9, that modification resulted in greater deflection values but did not come any closer to replicating the experimental result. The flatness of the modeled and FEA results is due to stiffening from beam stretch. For the beam (or plate) to deflect, it must also lengthen. The shape of the experimental curve suggests that the amount of strain stiffening is less than predicted. If we reduce the contribution of the beam stretch term in equation (14) by 90%, the predicted midpoint deflections match the experimental result well. Figure 9 shows this result, in which the 'beam stretch factor' (or BSF) is 0.1.

We conclude two things from the results in figure 9. First, our finite-element results do not adequately describe the deflections of the entire force loop (anchors, substrate); others have noted the significant effect of anchor compliance on actuator behavior [16, 17]. Second, the simple uniform load model becomes less accurate as midpoint deflection and residual stress increase.

4. Dynamic analysis

The goal of the dynamic analysis is to develop a simple model for estimating first mode natural frequency. The equations of motion can be derived using Lagrange's equation:

$$L = T - \pi. \tag{16}$$

The kinetic energy T is

$$T = \frac{1}{2} m'_{\text{beam}} \int_0^L \dot{x}^2 \, \mathrm{d}y, \tag{17}$$

where m'_{beam} is the mass per unit length of the beam. With a third-order expansion of the electrostatic potential energy

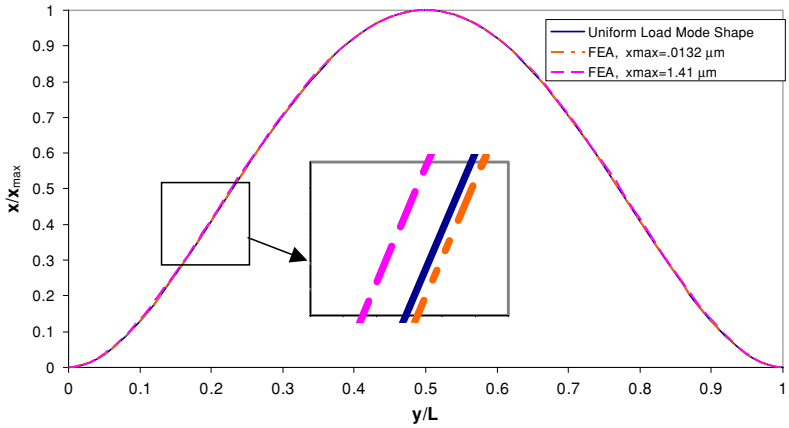

Figure 8. Comparison of uniform load mode shape to finite-element prediction.

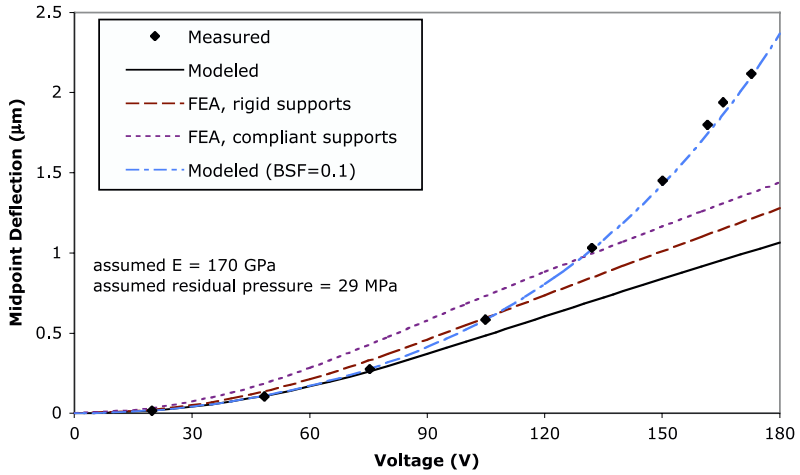

Figure 9. Comparison of measured and modeled static deflection for 5 μm gap actuator.

Table 3. Design dimensions for the experimentally tested micromirror with process standard deviation indicated for t and g_o.

Actuator material	Polysilicon
Actuator membrane width (w)	240 μm
Actuator membrane length (L)	240 μm
Actuator membrane thickness (t)	2 μm (σ = 26 nm)
Gap height (g_o)	5 μm (σ = 57 nm)
Mirror area	300 μm × 300 μm
Mirror layer thickness	3 μm
Post size	20 μm long, 2 μm wide and 2.5 μm high

term, π is

$$\pi = \frac{1}{2}EI\int_0^L (x'')^2\,\mathrm{d}y + \frac{1}{8}EA\int_0^L (x')^4\,\mathrm{d}y - \frac{1}{2}\int_0^L F_a(x')^2\,\mathrm{d}y - \frac{1}{2}\frac{\varepsilon_o w V^2}{g_o} \times \int_0^L \left(1 + \frac{x}{g_o} + \frac{x^2}{g_o^2} + \frac{x^3}{g_o^3}\right)\mathrm{d}y. \tag{18}$$

The dynamic mode shape, assuming one mode, is

$$x(y,t) = \phi(y)q(t). \tag{19}$$

The Lagrangian L is then

$$L = \frac{1}{2}m'_{\mathrm{beam}}\dot{q}^2\int_0^L \phi^2\,\mathrm{d}y - \frac{1}{2}EIq^2\int_0^L (\phi'')^2\,\mathrm{d}y - \frac{EA}{8}q^4\int_0^L (\phi')^4\,\mathrm{d}y + \frac{1}{2}F_a q^2\int_0^L (\phi')^2\,\mathrm{d}y + \frac{\varepsilon_o w V^2}{2g_o}\int_0^L \left(1 + \frac{\phi}{g_o}q + \frac{\phi^2}{g_o^2}q^2 + \frac{\phi^3}{g_o^3}q^3\right)\mathrm{d}y. \tag{20}$$

Applying Lagrange's equation

$$\frac{\mathrm{d}}{\mathrm{d}t}\left(\frac{\partial L}{\partial \dot{q}}\right) - \frac{\partial L}{\partial q} = 0, \tag{21}$$

the dynamic equation is

$$M\ddot{q} + Kq + \Gamma q^2 + \Psi q^3 = BV^2, \tag{22}$$

where

$$M = m'_{\mathrm{beam}}\int_0^L \phi^2\,\mathrm{d}y = \frac{m_{\mathrm{beam}}}{L}\int_0^L \phi^2\,\mathrm{d}y, \tag{23}$$

$$K = EI\int_0^L (\phi'')^2\,\mathrm{d}y - F_a\int_0^L (\phi')^2\,\mathrm{d}y - \frac{\varepsilon_o w V^2}{g_o^3}\int_0^L \phi^2\,\mathrm{d}y, \tag{24}$$

$$\Gamma = -\frac{3\varepsilon_o w V^2}{2g_o^4}\int_0^L \phi^3\,\mathrm{d}y, \tag{25}$$

$$\Psi = \frac{EA}{2}\int_0^L (\phi')^4\,\mathrm{d}y, \tag{26}$$

$$B = \frac{\varepsilon_o w}{2g_o^2}\int_0^L \phi\,\mathrm{d}y. \tag{27}$$

For the uniform load mode shape,

$$\phi(y) = y^4 - 2Ly^3 + L^2y^2. \tag{28}$$

Equations (23)–(27) become

$$M = \frac{m_{\mathrm{beam}}L^8}{630}, \tag{29}$$

$$K = \frac{4}{5}EIL^5 - \frac{2}{105}F_aL^7 - \frac{\varepsilon_o w V^2 L^9}{630g_o^3}, \tag{30}$$

$$\Gamma = -\frac{\varepsilon_o w L^{13}}{8008}V^2, \tag{31}$$

$$\Psi = \frac{4EAL^{13}}{15\,015}, \tag{32}$$

$$B = \frac{\varepsilon_o w L^5}{60g_o^2}. \tag{33}$$

At the beam's midpoint,

$$x_{L/2}(t) = \phi(L/2)q(t). \tag{34}$$

Substituting $L/2$ into equation (28) yields

$$\phi(L/2) = \frac{L^4}{16}. \tag{35}$$

Rearranging equation (34) and substituting for ϕ,

$$q(t) = \frac{16}{L^4}x_{L/2}(t). \tag{36}$$

Substituting for q and simplifying, the dynamic equation is now

$$m_{\text{beam}}\ddot{x}_{L/2} + \left(\frac{504EI}{L^3} - \frac{12F_a}{L} - \frac{\varepsilon_o wL}{g_o^3}V^2\right)x_{L/2} - \left(\frac{180\varepsilon_o wL}{143g_o^4}V^2\right)x_{L/2}^2 + \left(\frac{6144EA}{143L^3}\right)x_{L/2}^3 = \frac{21\varepsilon_o wLV^2}{32g_o^2}. \tag{37}$$

For comparison to the beam stiffness as described in equation (2), the dynamic equation is rewritten as

$$\frac{16}{21}m_{\text{beam}}\ddot{x}_{L/2} + \left(\frac{384EI}{L^3} - \frac{64F_a}{7L} - \frac{16\varepsilon_o wL}{21g_o^3}V^2\right)x_{L/2} - \left(\frac{960\varepsilon_o wL}{1001g_o^4}V^2\right)x_{L/2}^2 + \left(\frac{32\,768EA}{1001L^3}\right)x_{L/2}^3 = \frac{\varepsilon_o wLV^2}{2g_o^2}. \tag{38}$$

For small midpoint deflections, the $x_{L/2}^2$ and $x_{L/2}^3$ terms are neglected, and the natural frequency of the beam actuator is

$$\omega_n = \sqrt{\frac{\frac{384EI}{L^3} - \frac{64F_a}{7L} - \frac{16\varepsilon_o wL}{21g_o^3}V^2}{\frac{16}{21}m_{\text{beam}}}}. \tag{39}$$

The dynamic equation of motion can also be linearized for the case of small dynamic motions about a dc offset by setting $x_{L/2} = x_o + \delta x$ and $V = V_o + \delta V$. After discarding terms containing $(\delta x)^2$, $(\delta V)^2$ and $\delta x\delta V$, the equation of motion becomes

$$\frac{16}{21}m_{\text{beam}}\delta\ddot{x} + \left[\frac{384EI}{L^3} - \frac{64F_a}{7L} - \frac{16\varepsilon_o wL}{21g_o^3} \times \left(1 + \frac{1920}{1001}\frac{x_o}{g_o}\right)V_o^2 + \frac{98\,304EA}{1001L^3}x_o^2\right]\delta x = \frac{\varepsilon_o wL}{2g_o^2}\left(\delta V + 2V_o + \frac{64}{21}\frac{x_o}{g_o}V_o + \frac{3840}{1001}\frac{x_o^2}{g_o^2}V_o\right)\delta V, \tag{40}$$

and the natural frequency is

$$\omega_n = \sqrt{\frac{\frac{384EI}{L^3} - \frac{64F_a}{7L} - \frac{16\varepsilon_o wL}{21g_o^3}\left(1 + \frac{1920}{1001}\frac{x_o}{g_o}\right)V_o^2 + \frac{98\,304EA}{1001L^3}x_o^2}{\frac{16}{21}m_{\text{beam}}}}. \tag{41}$$

To use equation (41), the static midpoint deflection x_o must first be calculated as described in section 2. Note that the electrostatic terms (with V^2 in them) have a softening effect while the beam stretch terms (with EA) have a stiffening effect.

In the actual system, the actuator layer has a post at the center that supports a mirror above the actuator layer. Assuming that the mirror and post do not affect the beam's EI and that the mirror and post can be modeled with a point mass, the kinetic energy is then

$$T = \frac{1}{2}m'_{\text{beam}}\int_0^L \dot{x}^2\,\mathrm{d}y + \frac{1}{2}m_{\text{mirror}}\dot{x}_{L/2}^2. \tag{42}$$

After modifying the Lagrangian, equation (29) becomes

$$M = m_{\text{beam}}\frac{L^8}{630} + m_{\text{mirror}}\frac{L^8}{256}. \tag{43}$$

The effective mass is then

$$m_{\text{eff}} = \tfrac{16}{21}m_{\text{beam}} + \tfrac{15}{8}m_{\text{mirror}} \tag{44}$$

and

$$\omega_n = \sqrt{\frac{\frac{384EI}{L^3} - \frac{64F_a}{7L} - \frac{16\varepsilon_o wL}{21g_o^3}\left(1 + \frac{1920}{1001}\frac{x_o}{g_o}\right)V_o^2 + \frac{98\,304EA}{1001L^3}x_o^2}{\frac{16}{21}m_{\text{beam}} + \frac{15}{8}m_{\text{mirror}}}}. \tag{45}$$

5. Dynamic model validation

Dynamic behavior of a micromirror with the dimensions outlined in table 3 was measured with a laser Doppler velocimeter. Figure 10 shows the measured frequency responses at dc offset voltages ranging from 0 to 125 V. The damped resonant frequency decreases from 68 to 64 kHz (a 6% reduction). Because the air pressure was low (3 Torr) in these tests, squeeze film effects should play a negligible role.

Resonant frequency was predicted using equation (45). Figure 11 shows resonant frequency as a function of offset voltage. At low voltages, resonant frequency decreases with increasing voltage. However, at higher voltages, strain stiffening causes the resonant frequency to increase. The absence of the strain stiffening effect in the experimental data suggests that unmodeled compliance in the force loop is counteracting the predicted stiffening effect. Inserting a coefficient of 0.1 in front of the EA/L term in equation (45) produces predictions closer to the experimental values. These are shown as the dotted line in figure 11.

6. Squeeze film effects

The air between two parallel plates can vent to dampen energy or compress to store energy. At low speeds, when air has time to escape, the air film dampens motions. At high speeds, when the air has less time to escape, the air film acts as a spring. The micromirrors in our application have a fixed–fixed deformable plate as the actuator layer. Modeling the effects of the squeeze film layer on this type of plate or beam is complex (see, for example, [15]). We investigated the utility of a simpler rigid beam model for our system. Thus, the squeeze film spring and damper (k_{air} and b_{air}) are modeled in parallel with the flexure spring k_{flex} and the inherent material damping $b_{\text{mat'l}}$ as shown in figure 12. Note that k_{air} and b_{air} are functions of frequency and gap g.

For k_{air} and b_{air} we adopt the model of Darling [14]. For parallel plates with venting on two opposite sides, the reaction force on the plate due to motion through the air is

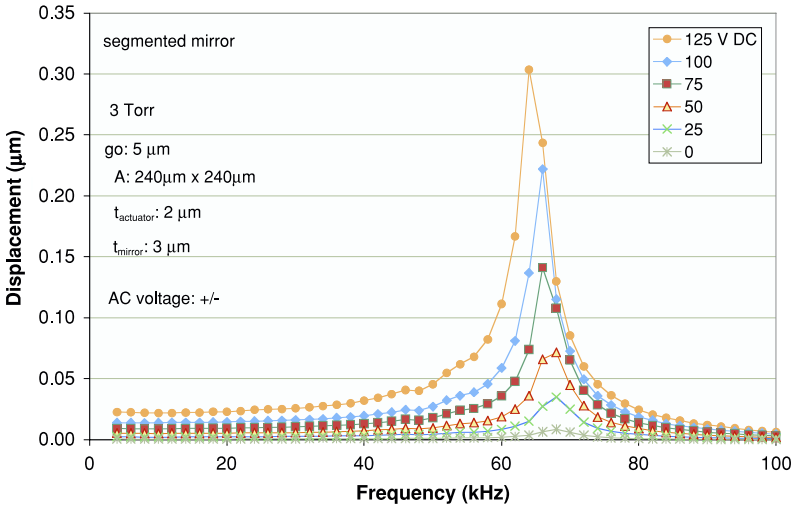

Figure 10. Experimental frequency responses of the micromirror at six different offset voltages.

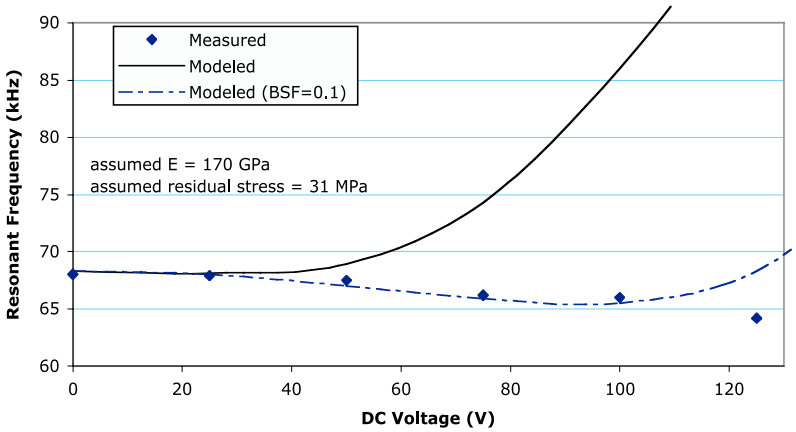

Figure 11. Effect of offset voltage on resonant frequency.

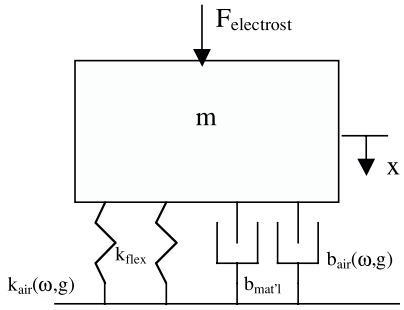

Figure 12. Lumped parameter model of the electrostatic actuator in air.

$$F = -\frac{8\mathrm{j}\omega x}{\pi^2 g_{\mathrm{avg}}}(L w p_{\mathrm{amb}}) \sum_{n=\mathrm{odd}} \frac{1}{n^2\left(\mathrm{j}\omega + k_n^2/\alpha^2\right)}, \tag{46}$$

where

$$\alpha^2 = \frac{12\mu}{g_{\mathrm{avg}}^2 p_{\mathrm{amb}}} \tag{47}$$

and

$$k_n^2 = \frac{n^2\pi^2}{w^2} \tag{48}$$

and where p_{amb} is the ambient air pressure, L is the length of plate, w is the width of plate, x is the plate displacement, g_{o} is the nominal gap and μ is the gas (air) viscosity. The spring component of this force is the real part while the damping component is the imaginary part. Thus,

$$k_{\mathrm{air}} = \frac{\mathrm{Re(F)}}{x}, \tag{49}$$

$$b_{\mathrm{air}} = \frac{\mathrm{Im}(F)}{x\omega}, \tag{50}$$

or

$$k_{\mathrm{air}} = \frac{1152\mu^2\omega^2 L}{\pi^2 p_{\mathrm{amb}}}\left(\frac{w}{g_{\mathrm{avg}}}\right)^5 \sum_{n=\mathrm{odd}} \frac{1}{n^2}\frac{1}{n^4 + \left(\frac{\omega}{\omega_{\mathrm{c}}}\right)^2}, \tag{51}$$

$$b_{\mathrm{air}} = \frac{96\mu L}{\pi^4}\left(\frac{w}{g_{\mathrm{avg}}}\right)^3 \sum_{n=\mathrm{odd}} \frac{1}{n^4 + \left(\frac{\omega}{\omega_{\mathrm{c}}}\right)^2}, \tag{52}$$

where ω_{c}, the cut-off frequency, is

$$\omega_{\mathrm{c}} = \frac{\pi^2 p_{\mathrm{amb}}}{12\mu}\left(\frac{g_{\mathrm{avg}}}{w}\right)^2. \tag{53}$$

When $\omega \ll \omega_{\mathrm{c}}$, the viscous force dominates over the spring force. When ω approaches ω_{c}, the spring forces become significant and cannot be neglected.

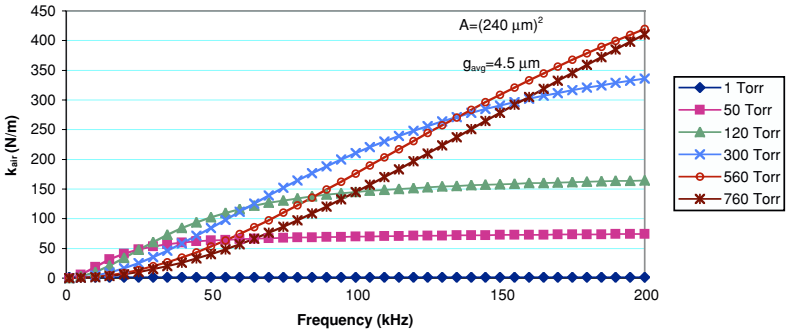

Figure 13. Stiffness of squeezed air film.

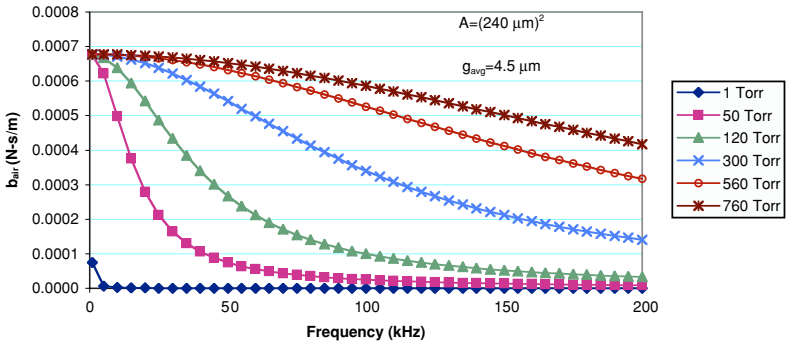

Figure 14. Damping due to squeezed air film.

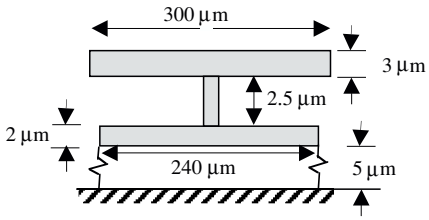

Let $k_{\text{flex}} = 160$ N/m

Figure 15. Micromirror design with rigid actuator layer.

Figures 13 and 14 show how k_{air} and b_{air} change with frequency and air pressure according to Darling's model. The following parameter values were used: $\mu = 1.862 \times 10^{-5}$ N s m^{-2}, $g_{\text{avg}} = 4.5$ μm, $L = w = 240$ μm. The first six terms of the summation (up to $n = 11$) were used. According to figure 13, k_{air} increases with frequency and eventually reaches a steady state. The steady-state (maximum) stiffness increases with ambient pressure. As shown in figure 14, damping decreases with frequency. It decreases most rapidly at low pressures. Because the model described above applies only to flat parallel plates, it can be most readily applied to a micromirror design with a rigid actuator layer as shown in figure 15.

Damped natural frequency for this design can be found as follows:

$$f_{\text{d}} = \frac{1}{2\pi}\omega_{\text{d}}, \tag{54}$$

$$\omega_{\text{d}} = \omega_n\sqrt{1-\zeta^2}, \tag{55}$$

$$\omega_n = \sqrt{\frac{k_{\text{eff}}(\omega)}{m}}. \tag{56}$$

The damping coefficient is

$$\zeta = \frac{b_{\text{mat'l}} + b_{\text{air}}(\omega)}{2m\omega_n}. \tag{57}$$

The effective stiffness is found by linearizing the equation of motion around a dc offset. The equation of motion (with a second-order expansion of the electrostatic force) is

$$m\delta\ddot{x} + \left[k_{\text{flex}} + k_{\text{air}} - \frac{\varepsilon_{\text{o}} w L V_{\text{o}}^2}{(g_{\text{o}} - x)^3} - \frac{3\varepsilon_{\text{o}} w L V_{\text{o}}^2 \delta x}{2(g_{\text{o}} - x_{\text{o}})^4}\right]\delta x = \frac{\varepsilon_{\text{o}} w L V_{\text{o}}}{(g_{\text{o}} - x_{\text{o}})^2}\delta V + \frac{\varepsilon_{\text{o}} w L}{(g_{\text{o}} - x_{\text{o}})^2}(\delta V)^2. \tag{58}$$

The effective stiffness is

$$k_{\text{eff}} = k_{\text{flex}} + k_{\text{air}} - \frac{\varepsilon_{\text{o}} A V_{\text{o}}^2}{2(g_{\text{o}} - x_{\text{o}})^2}\left[\frac{2}{g_{\text{o}} - x_{\text{o}}} + \frac{3}{(g_{\text{o}} - x_{\text{o}})^2}\delta x\right]. \tag{59}$$

If a first-order expansion were assumed, the stiffness would be

$$k_{\text{eff}} = k_{\text{flex}} + k_{\text{air}} - \frac{\varepsilon_{\text{o}} A V_{\text{o}}^2}{(g_{\text{o}} - x_{\text{o}})^3}. \tag{60}$$

Note that ω_{d} depends on k_{air} and b_{air}. However, k_{air} and b_{air} depend on ω. Thus, some iteration is required to find k_{air}, b_{air} and ω_{d}. Table 4 shows estimates of damped natural frequency calculated using equations (51)–(57) for the case of $V_{\text{o}} = 80$ V ($x_{\text{o}} = 501$ nm). The effective stiffness k_{eff} is calculated assuming a zeroth-order electrostatic force expansion (first two terms of equation (59)) and with first- and second-order expansions (equations (60) and (59), respectively). Note that pressure causes significant increases in the damped natural frequency. As pressure increases, k_{air} and b_{air} grow larger than k_{flex} and $b_{\text{mat'l}}$. The table results suggest that the first-order approximation for electrostatic force is sufficient in this case.

Table 4. Estimates of damped natural frequency that include squeeze film effect and electrostatic force correction. Conditions: $L = w = 240\ \mu$m, $k_{flex} = 160$ N m^{-1}, $m = 7.0 \times 10^{-10}$ kg, $g_o = 5\ \mu$m, $V = 80 \pm 1$ V ($x_o = 0.501\ \mu$m, $\delta x = 16$ nm at low frequencies), $b_{mat'l} = 2 \times 10^{-5}$ N s m^{-1}.

p (Torr)	f_d (kHz) (zeroth order)	f_d (kHz) (first order)	f_d (kHz) (second order)	k_{air} (N m^{-1})	b_{air} (N s m^{-1})
0	76.1	67.1	67.1	0	0
1	76.5	67.5	67.5	1.64	8.8×10^{-8}
50	91.0	83.4	83.3	68.6	3.3×10^{-5}
120	104.6	97.6	97.5	144	1.0×10^{-4}
300	114.8	104.5	104.4	220	3.3×10^{-4}

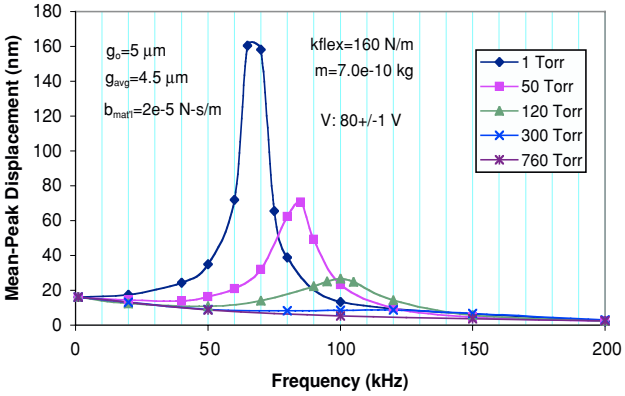

Figure 16. Simulated frequency response showing the effect of air pressure.

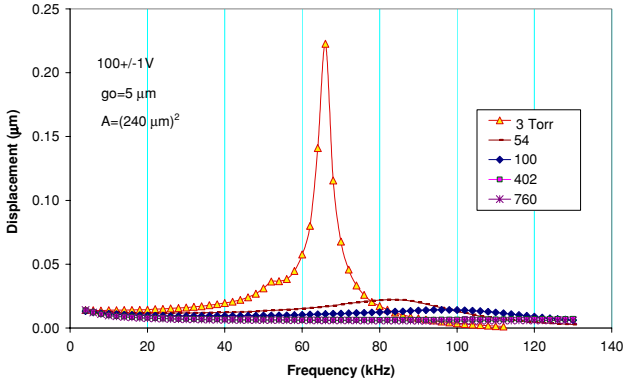

Figure 17. Measured frequency response of the micromirror at five different ambient pressures.

A Simulink model that incorporates the exact (no binomial approximation) nonlinear electrostatic forcing function was used to generate time response data for a sinusoidal voltage input. The composite k ($k_{air} + k_{flex}$) and b ($b_{air} + b_{mat'l}$) were changed each time the input frequency was changed based on the above relations. The magnitude of the displacement output was recorded over a range of frequencies as shown in figure 16. Note that the peak frequencies agree with those in table 4.

A micromirror was placed in a small benchtop vacuum chamber with a viewing window. Dynamic behavior was again measured using a laser Doppler velocimeter. Figure 17 shows frequency response for five different ambient pressures at a dc offset voltage of 100 V. The damped resonant frequency increases from 66 to 96 kHz (45% increase) when the ambient pressure increases from 3 to 100 Torr. At 402 and 760 Torr, the system is overdamped and presents no resonant peak. At 100 V dc offset and 3 Torr ambient pressure, the model described above predicts a damped resonant frequency of 66 kHz if k_{flex} is set to 183 N m^{-1}. With that k_{flex} at 100 Torr, the model predicts a resonant frequency of 95 kHz (very close to the 96 kHz of the actual micromirror). The similarity in the actual and predicted effects suggests that the rigid actuator squeeze film model can give useful design information for fixed–fixed deformable beams.

The squeeze film also causes interesting step response behavior. Veijola *et al* [11] developed a model for predicting frequency and step response of a silicon accelerometer as a function of gas pressure. The step response at 300 Pa has some unusual behavior: a fast initial response is followed by a slower rise to the final value. When first actuated, the gas film acts mostly as a spring thus giving the system a high bandwidth

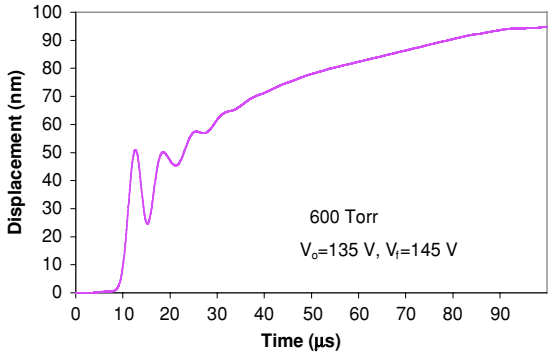

Figure 18. Measured step response of the micromirror.

and fast response. After the first millisecond, however, the gas film has a dampening effect. We observed similar behavior when testing micromirrors. Figure 18 shows step response as measured by laser Doppler velocimeter. The mirror was actuated by a square wave oscillating between 135 and 145 V.

7. Conclusions

Many models have been developed by others to describe the static and dynamic behaviors of parallel-plate electrostatic actuators. Our goal was to develop and/or adopt models that are convenient to use in the design of MEMS spatial light modulators. For predicting static deflection, our model requires only that the roots of a third-order equation be found (see equations (14) and (15)). The natural frequency assuming small motions about a dc offset can be calculated quickly using equation (45). Finally, the effect of ambient pressure on natural

frequency and damped natural frequency can be approximated from equations (51)–(57) and (60).

The static model results match FEA predictions closely except at the highest displacements where the model underpredicts displacement. Relative to actual device displacement, both the analytical model and FEA underpredict displacement at high displacement levels. In other words, the actual device does not exhibit as much stiffness as predicted at high displacements. This appears to be due to unmodeled compliance in the force loop. By limiting the amount of stiffening introduced by beam stretch, the model can be matched to the experimental data.

The natural frequency of the real devices decreases as dc offset voltage increases. The dynamic model includes two competing effects: stiffening due to beam stretch (which tends to increase natural frequency) and softening due to the nonlinear electrostatic force (which tends to decrease it). The analytical model agrees with experiment only if the beam stretch contribution is reduced by the same amount as described above for the static case.

Squeeze film effects were determined by adopting a model that had been developed for rigid parallel plates. Although the actuator plates in the real devices bend, the rigid plate model adequately predicts the effect of ambient pressure on damped natural frequency.

Acknowledgment

The work described in this paper was supported by the Defense Advanced Research Projects Agency through the Coherent Communications, Imaging and Targeting (CCIT) program.

References

[1] Tilmans H A C and Legtenberg R 1994 Electrostatically driven vacuum-encapsulated polysilicon resonators: II. Theory and performance *Sensors Actuators* A **45** 67–84

[2] Choi B and Lovell E G 1997 Improved analysis of microbeams under mechanical and electrostatic loads *J. Micromech. Microeng.* **7** 24–8

[3] Najar F, Choura S, El-Borgi S, Abdel-Rahman E M and Nayfeh A H 2005 Modeling and design of variable-geometry electrostatic microactuators *J. Micromech. Microeng.* **15** 419–29

[4] Abdel-Rahman E M, Younis M I and Nayfeh A H 2002 Characterization of the mechanical behavior of an electrically actuated microbeam *J. Micromech. Microeng.* **12** 759–66

[5] Chowdhury S, Ahmadi M and Miller W C 2005 A closed-form model for the pull-in voltage of electrostatically actuated cantilever beams *J. Micromech. Microeng.* **15** 756–63

[6] Ananthasuresh G K, Gupta R K and Senturia S D 1996 An approach to macromodeling of MEMS for nonlinear dynamic simulation *ASME IMECE* DSC-59 pp 401–7

[7] Mehner J E, Gabbay L D and Senturia S D 2000 Computer-aided generation of nonlinear reduced-order dynamic macromodels: II. Stress-stiffened case *J. Microelectromech. Syst.* **9** 270–8

[8] Younis M I, Abdel-Rahman E M and Nayfeh A 2003 A reduced-order model for electrically actuated microbeam-based MEMS *J. Microelectromech. Syst.* **12** 672–80

[9] Seidel H, Riedel H, Kolbeck R, Muck G, Kupke W and Koniger M 1990 Capacitive silicon accelerometer with highly symmetrical design *Sensors Actuators* A **21–23** 312–5

[10] Andrews M, Harris I and Turner G 1993 A comparison of squeeze-film theory with measurements on a microstructure *Sensors Actuators* A **36** 79–87

[11] Veijola T, Kuisma H, Lahdanpera J and Ryhanen T 1995 Equivalent-circuit model of the squeezed gas film in a silicon accelerometer *Sensors Actuators* A **48** 239–48

[12] Yang Y-J, Gretillat M-A and Senturia S D 1997 Effect of air damping on the dynamics of nonuniform deformation of microstructures *Transducers '97* pp 1093–6

[13] Hung E S, Yang Y-J and Senturia S D 1997 Low-order models for fast dynamical simulation of MEMS microstructures *Transducers '97* pp 1101–4

[14] Darling R B, Hivick C and Xu J 1998 Compact analytical modeling of squeeze film damping with arbitrary venting conditions using a Green's function approach *Sensors Actuators* A **70** 32–41

[15] Nayfeh A H and Younis M I 2004 A new approach to the modeling and simulation of flexible microstructures under the effect of squeeze film damping *J. Micromech. Microeng.* **14** 170–81

[16] Baker M S, de Boer M P, Smith N F, Warne L K and Sinclair M B 2002 Integrated measurement-modeling approaches for evaluating residual stress using micromachined fixed–fixed beams *J. Microelectromech. Syst.* **11** 743–53

[17] Park Y-H and Park K C 2004 High-fidelity modeling of MEMS resonators *J. Microelectromech. Syst.* **13** 348–57